ELSEVIER

Hot-film anemometry in bubbly flow I: bubble–probe interaction

Judith Rensen, Stefan Luther [*], Joris de Vries, Detlef Lohse

Department of Science and Technology and J.M. Burgers Center for Fluid Dynamics, University of Twente, P.O. Box 217, 7500 AE Enschede, The Netherlands

Abstract

The interaction between a bubble, which is rising in a descending water flow, and a hot-film anemometer was experimentally investigated using stereoscopic high-speed imaging. The mean downward water velocity varied from 0 up to 0.15 m/s, i.e., relatively low, allowing for an extended bubble–probe interaction. Moreover, the direction of the water causes the wake of the probe to play a role before the bubble touches the probe. The equivalent bubble radii were 0.4–2.8 mm and the bubble velocities relative to the probe ranged from 0.04 to 0.38 m/s. Image processing techniques were applied to reconstruct the bubbles' path, shape, and orientation during the interaction process. As a result, three types of interactions were found, namely penetrating, bouncing, and splitting interactions. The image sequences were compared with the corresponding time series of the hot-film anemometer. From the time series the type of interaction cannot be deduced, at least not for the analyzed flow situation. Furthermore, we demonstrated that the residence time estimate from the hot-film data is systematically biased in our type of experiments. Finally, it was found that the velocity of a bubble may be altered considerably due to the interaction.

---

[*] Corresponding author.
E-mail address: s.luther@tnw.utwente.nl (S. Luther).

1. Introduction

One of the most frequently used techniques to perform velocity measurements in fluids is hot-film anemometry (Goldstein, 1996). This technique is based on the relation between the heat flux from an electrically heated sensing element, which is placed in a flow, and the local fluid velocity. Also in bubbly flow this technique has been applied by many researchers (Delhaye, 1969; Herringe and Davis, 1974; Lance and Bataille, 1991; Farrar and Bruun, 1996; Liu, 1997; Wang and Ching, 2001).

An advantage of this technique is that it has a high-upper frequency limit in bubbly flow as compared to laser Doppler anemometry (LDA) or particle image velocimetry (PIV). Especially in the case that measurements far from a wall are required, these optical techniques suffer from low data rates due to blocking of the optical path by bubbles. However, there are also some disadvantages associated with hot-film anemometry. The most important disadvantage is that it is an intrusive technique. As a consequence not only the water flow and the bubbles' paths are affected, but also spiky structures occur in the hot-film signal. These spiky structures are caused by the decrease in heat loss of the probe when a bubble touches the sensitive part of the probe, due to the low heat capacity of air as compared to water. As the spikes do not contain any information on the water velocity, they need to be separated from the rest of the signal. To be able to identify them, one needs to know their typical shapes. This is one of the reasons why bubble–probe interactions have been investigated by various researchers (Delhaye, 1969; Herringe and Davis, 1974; Bremhorst and Gilmore, 1976; Serizawa et al., 1983). Another reason to investigate the interactions is to explore the possibility to use the disturbances themselves to obtain information on the bubbles, like e.g. gas fractions, bubble sizes, and velocities. In their research Hamad and Bruun (2000) and Wang and Ching (2001) have demonstrated that it is possible to obtain the velocity of bubbles from hot-film signals. However, in those papers the bubbles and the flow either had the same direction, i.e. both ascending or both descending, or the tests were performed in quiescent water. Here, in contrast, we want to apply hot-film anemometry in a situation in which water is descending while bubbles rise upwards. Such flow geometry results in a lower relative velocity of the bubble with respect to the probe, and therefore allows for a longer interaction process. The analyzed type of probe is a cylindrical hot-film probe. We were particularly interested in the shape of the bubbly spikes and the changes in the path of the bubbles due to the interaction. Besides, we wanted to investigate whether measurements of the gas fraction with a hot-film probe were still possible for this flow situation with reduced relative bubble velocity and an influence of the wake of the probe before the interaction.

In order to study the interaction, we performed hot-film measurements in a water tunnel in which single bubbles were rising in a downward directed water flow or in quiescent water. We applied stereoscopic high-speed imaging to visualize the interaction. Another new aspect of our research compared to earlier work was that we applied an image processing algorithm that reconstructs the three-dimensional shape of the bubbles. This algorithm has been successfully applied previously (Luther et al., 2004). Due to the three-dimensional reconstruction, an accurate determination of the size, the position and the orientation of bubbles was possible.

This paper is organized as follows. In Section 2 the experimental setup is described. Section 3 introduces the signal processing. The results can be found in Section 4. Our conclusions are discussed in Section 5.

2. Experimental setup

2.1. Water tunnel and bubble injection

The water tunnel is depicted in Fig. 1(a). The water flow is directed vertically downwards in the test section, which has a cross section of 8×8 cm^2. Bubbles are injected at the bottom of the test section 25 cm below the probe and rise against the water flow. Rising in the liquid, they eventually hit the probe, i.e. the film and/or the prongs. Whenever this happened, the data was stored. Additionally, some gliding events or close-to collisions have been recorded. The size of the bubbles was controlled by means of an electronically triggered valve. The equivalent bubble radii are in the range 0.4–2.8 mm.

2.2. Hot-film anemometer

We used a Dantec constant temperature anemometer system and a Dantec 55R11 hot–film probe. The probe was mounted in the test section under an angle of 45° (see Fig. 1(b)). The probe consists of a cylindrical quartz rod of 70 μm diameter and 3 mm length, with a sensitive length of 1.3 mm. The overheat ratio is 0.1 corresponding to an over temperature of about 30 °C. The signal of the hot-film probe was digitized with a sampling rate of 6 kHz and a resolution of 12 bit (National Instruments BNC-2090 and PCI-E6023).
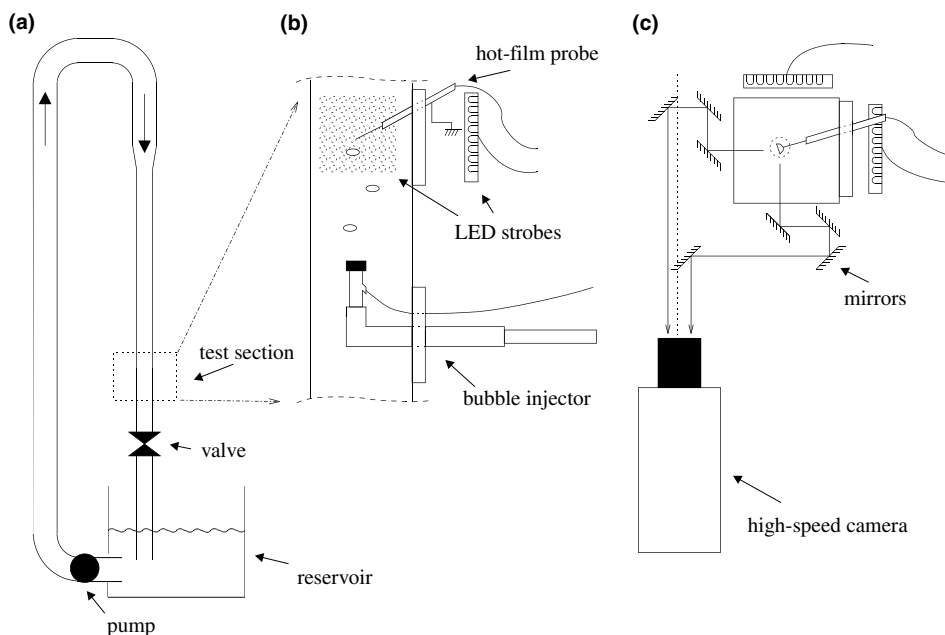

Fig. 1. Experimental setup. (a) Water channel with circulatory flow. (b) Enlargement of the test section. (c) Optical path for stereoscopic imaging (top view).

2.3. Stereoscopic imaging

The components for the stereoscopic imaging setup are shown in Fig. 1(c). It consists of a high-speed camera (Kodak CR Imager 2000), a beam splitter, and the illumination. The high-speed camera has a maximum frame rate of 2000 frames per second with a resolution of 144×512 pixels. The beam splitter provides two orthogonal views of the measurement volume, which has a size of $2 \times 2 \times 2 \, cm^3$. For illumination, we used arrays of light emitting diodes (LEDs). These were operated in stroboscopic mode with a flash duration of 23 µs. This light source provided homogeneous intensity and good contrast without heating up the test section. The optical setup was calibrated for spatial reconstruction using a calibration grid with a spacing of 2 mm. To perform the mapping of the three-dimensional scene onto the two-dimensional images the camera model described by Tsai (1987) was used. This model accounts for optical and electronic distortions during image capture. The model's parameters were calibrated in a least square sense. As a result a reconstruction error of 27 µm with a standard deviation of 11 µm was obtained.

During the experiment, the camera and the hot-film continuously acquired data into circular buffers. When they were triggered on the rising edge of the hot-film signal, data from a time window of 0.1 s was stored centered around the trigger event. Therefore, data is obtained for the approach of the bubble, its interaction with the probe, and its departure. No pre-selection of the interaction events was done. Therefore, the impact conditions are essentially random. Due to the relative large number of events, we assume these results to be representative for the experimental conditions under consideration.

3. Data analysis

3.1. Image processing

The image processing consists of five steps: image pre-processing, object recognition, reconstruction of the three dimensional position and shape, object tracking, and post-processing.

Image pre-processing: A background image was selected, which did not contain bubbles. This image was subtracted from the other images of the sequence. In this way the influence of inhomogeneities in the illumination as well as the image of the hot-film probe were removed.

Object recognition: A gray level threshold was defined, which segmented the image in a bubble part and a water part, respectively. The threshold for a gray level image I is

$$\frac{I - I_{min}}{I_{max} - I_{min}} = 0.55, \tag{1}$$

where I_{max} and I_{min} are the image gray values at the center of the object and far away, respectively. The threshold value of 0.55 can rigourously be derived for the image of an opaque disk and a finite aperture optical system. It was found to yield accurate results for images of blurred bubbles when compared with calibration targets.

The obtained binary image was labelled, i.e. adjacent pixels were clustered into regions. The centroid, the minor and major axes, the area, and the orientation of the bubble *images* can be obtained from the moments of this segments. However, these shape descriptors refer to the bubble's image, but not the bubble. In general, the geometry of the projected non-spherical bubble image does not allow to infer the shape or location of the bubble itself. Therefore, the bubble shape and location are obtained from a algorithm that takes into account the three dimensional shape of the bubble and the perspective mapping of the imaging system. This stereoscopic contour matching approach is described below.

During interaction of the bubble with the probe, the bubble is partially occluded by the probe. Thus, removing the background image, the bubble's image is 'cut' into one or more fragments. This problem was solved by using so called active contours, which approximate an object's contour line by an energy minimizing spline (Kass et al., 1987). The spline approach provides an easy way to capture the shape of this segmented object. To do so, we initialize the active contour with a circle including all segments. As the contour propagates, it finally approaches the contour of the bubble. The stiffness of this spline can be chosen such that it does not follow the gaps in between segments. The vertices of the spline representation of the bubble's contour provides the input to the three dimensional reconstruction.

3D reconstruction: The measurement of the bubble shape based on its two dimensional projections is in general intricate. If a bubble is not rising straight but tilted with respect to the image planes, one cannot directly extract its shape from the contour lines in the stereoscopic images. Nevertheless, the reconstruction from stereoscopic images is feasible provided that the shape obeys some constraints. Our approach is based on contour-matching methods (Cipolla, 1998). It assumes the bubble shape being ellipsoidal, but allows for a flattening of the rising bubble (Luther et al., 2004). The ellipsoidal shape is defined by the position of its center, its major and minor axes, and by the rotation of its symmetry axes with respect to the world coordinate system. The contour lines of a bubble described by this model are obtained by applying the camera model, i.e. by projecting or mapping the bubble onto the stereoscopic image plane. To find the model parameters of a observed bubble, the discrepancy between modelled and experimental contour lines was minimized in a least square sense by adapting the parameters of the bubble model (Press et al., 1992). Hence, the minor and major axes of the bubble are defined by the ellipsoid that reproduces the observed image contours in a least square sense. The distances between the modelled and the reconstructed contour lines were determined for typically 65 vertices of the contour. The average of these distances was used as a measure of the error in the estimate of the bubble surface positions and therefore also as an error in the estimate of the minor and major axis. The reconstruction of the bubble parameters is illustrated in Fig. 2. The bubbles shape and position obtained in this 3D reconstruction step are used to track the bubbles.

Object tracking: The bubbles were tracked in the world coordinate system using a multiple–frame tracking algorithm. Typically, 10–15 frames prior to the bubble impact on the probe are used. The trajectory of the bubbles is denoted by $x(t)$. The instantaneous velocity $v(x, t)$ is obtained by fitting a straight line to a neighborhood of five consecutive positions centered at $x(t)$. The least square fit is most easily done by computing the eigenvalues of the tensor of inertia of the corresponding five bubble positions. The error in this velocity measurement is estimated using the standard deviation of the discrepancy between the measured positions of data points and their corresponding fits.
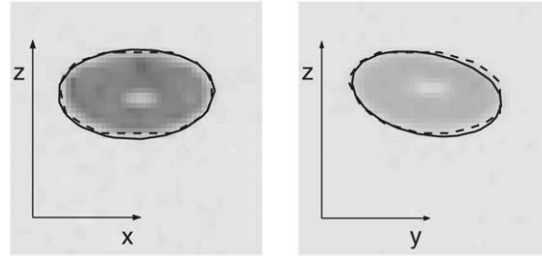
Fig. 2. The two stereoscopic views of a bubble, which has a major axis of 1.3 mm, a minor axis of 0.7 mm, and an equivalent radius of 1.5 mm, calculated from the 3D-reconstruction. The figure shows the two corresponding stereoscopic images after background subtraction. The dashed lines indicate the found contour lines. The solid lines indicate the contour lines of the reconstructed bubble. The contrast of the images was reduced to make the contour lines visible.

3.2. Bubble residence time estimation from the hot-film data

One of the questions we would like to answer in this paper is the suitability of a hot-film probe to measure the gas fraction. To obtain the gas fractions, the residence times of the bubbles that hit the sensing element of the hot-film probe are needed. These residence times can be obtained from the hot-film signal. A typical hot-film signal during bubble–probe interaction is depicted in Fig. 3. It has been argued by Serizawa et al. (1983), Bruun (1995), and Hamad and Bruun (2000) that the residence time of a bubble on the probe is given by the time interval between point *a* and *b*. The *local* gas fraction is then estimated by the fraction of the sum of the residence times of all bubble–probe interactions during the total measurement time *T*, i.e.

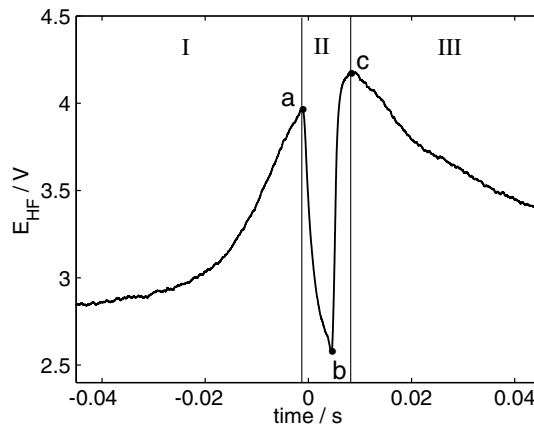$$\alpha = \sum_{i=1}^{N} \frac{\Delta t_{ab,i}}{T}, \tag{2}$$

Fig. 3. A hot-film signal E_{HF} vs. time during a bubble–probe interaction. At point *a* the bubble front hits the hot-film probe, resulting in a steep decrease of the signal. The signal then further decreases till the back of the bubble arrives at point *b*. Then the hot-film gets into contact with the water flow again, which leads to a strong increase of the signal up to point *c*. The parts I, II, and III refer to the pre-contact, the contact, and the post-contact stages of the signal as described in Section 4.2.

where N is the number of bubble–probe interactions during the measurement, $\Delta t_{ab,i}$ is the residence time of the ith bubble in the hot-film signal. Two effects bias the measurement of the void fraction as defined by Eq. (2). First, above definition of the local void fraction assumes a pointwise measurement, whereas the probe is spatially extended. The effective cross section does not only include the sensitive area but also the prongs of the probe. Thus, the effective size of the probe and the bubble size are of the same order. Second, the motion of the bubbles are significantly changed during the collision with the probe. The bubbles' path and shape may change, which will effect the residence times $\Delta t_{ab,i}$. To study the influence of the disturbances of the probe on the residence time we compared the residence time estimate from the hot-film signal with the residence time that one would expect if the bubble is not disturbed by the probe. In the next section we explain how we obtained this latter estimate.

3.3. Bubble residence time estimation from the high-speed images

We compared the residence times of bubbles on the probe obtained from the hot-film signal (see Section 3.2) with the residence times one would expect taking into account the bubble size, position and velocity just before the interaction to investigate the correctness of the first estimate. These experimental parameters were obtained by the analysis of the high-speed images, which were recorded simultaneously with the hot-film signals. They provide the input for a simple geometric model predicting the expected residence times, if the bubble's motion would not be affected by the presence of the probe. The model further assumes that the bubble has an ellipsoidal shape, and that it is moving in the direction of its axis of symmetry. In the model the sensing element is described as a line segment between the two prongs. The prong positions were obtained from the image analysis. The fact that the sensing element is only part of the rod between the two prongs was taken into account. The residence time is obtained by calculating the time interval between the time at which the bubble first touches the sensing element of the hot-film probe and the time at which it leaves the probe. To simplify the calculation we used a frame of reference in which the bubble is located at the origin with its axis of symmetry aligned with the vertical axis along which the probe is moving. To obtain the velocity, the size and the position of a bubble the last 15 frames before point a (see Fig. 3) were used. The velocity was obtained by the tracking algorithm described in Section 3.1. The estimate of the size and the position were obtained by averaging the results of the 15 images. The accuracy of the resulting residence time estimate depends on the accuracy of the estimate of the bubble size, position and velocity obtained by the image analysis and the accuracy of the determination of the probe position. We estimated the error in the obtained residence times taking the inaccuracy of these measures into account.

4. Results

In total we have obtained image sequences and hot-film signals of 153 bubble–probe interactions. The equivalent radii r_{eq} and the rise velocities V_{in} relative to the probe of bubbles for which the error in the size estimate of the equivalent radius was smaller than 0.1 mm are shown in Fig. 4.
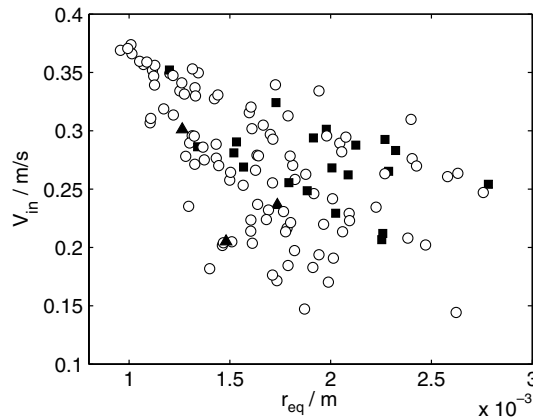
Fig. 4. The different types of interactions as function of the equivalent bubble radius r_{eq} and the collision velocity V_{in}. The bouncing interactions are denoted by circles, the splitting interactions by squares, and the penetrating interactions by triangles. No correlation between velocity or bubble radius with the type of interaction can be recognized.

4.1. Image analysis: types of interaction

The images of the bubble–probe interactions were classified into three groups: penetrating, splitting, and bouncing interactions. Fig. 5 displays image sequences for these three types. These classes correspond to the results of Serizawa et al. (1983) and Benk et al. (2001), though these authors found a fourth interaction type, namely glancing bubbles. As it is not possible to strictly discriminate between glancing and bouncing hits, we merged these two types. For all types of interaction we observed that the bubble first folds around the probe. From this point the interaction goes on in one of three different ways:

- *Penetrating bubble:* The two bulges meet each other and merge. The sensitive part of the probe is then inside the bubble, till the back end of the bubble has passed the probe.
- *Splitting bubble:* The notch that originates from the folding of the bubble gets deeper, till the back end of the bubble hits the probe. As a consequence, the two bulges break up into two separate bubbles.
- *Bouncing bubble:* One of the two bulges is pulled back under the probe and the bubble leaves the probe on one side.

Images of the three different types of interaction are depicted in Fig. 5. These images show that the bubbles are strongly deformed during the interaction. Even when a bubble has already left the probe, shape deformations can be present, see also Benk et al. (2001). These surface oscillations, which originate from the bubble–probe interaction, are sometimes very strong. For more details on the surface oscillations and for their implication on the rise velocity we refer to de Vries et al. (2002).

From Fig. 4 it is evident, that there is no correlation between the velocity or the bubble radius with the type of interaction. Furthermore this figure indicates that for the velocity and bubble size ranges considered in this paper, bouncing is found to be most probable, while splitting is less
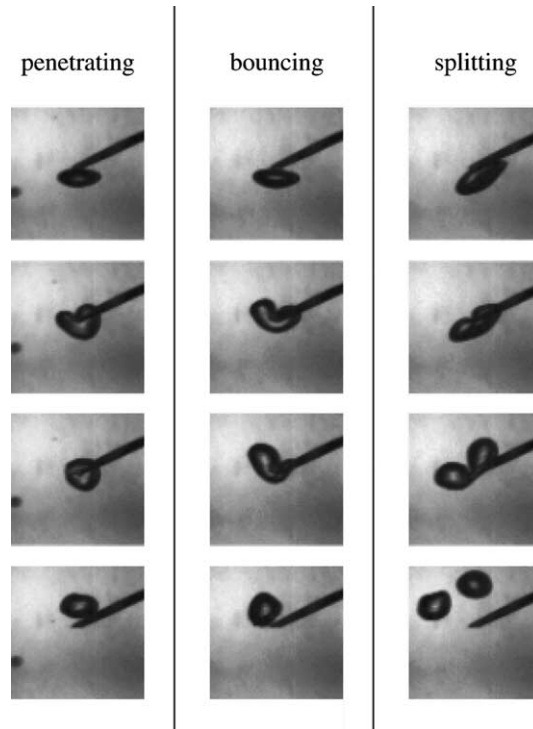
Fig. 5. Left: image sequence of a penetrating bubble–probe interaction. Middle: image sequence of a bouncing bubble–probe interaction. Right: image sequence of a splitting bubble–probe interaction.

probable, and penetration is rare. This finding is in remarkable contrast to the results reported for co-flow conditions. There, the penetrating bubble interaction is found to be most likely. The differences between co- and counter-current conditions are: (i) the impact velocity of the bubble on the probe (which is usually smaller in counter-current conditions); (ii) wake effects disturbing the bubble approach (which occur in counter-current conditions only). Thus, the flow distortion due to the probe's wake could explain why bouncing is most likely in the counter-current case, and in turn, suggest that penetration becomes more likely, if the bubbles approach in an undisturbed flow field, i.e. the co-current condition. However, a detailed comparison of co- and counter-flow conditions is beyond the scope of this paper.

4.2. Hot-film signal

In Fig. 6 different bubble–probe interaction signals can be seen. As illustrated by this figure there is quite some variety in the shapes of the signals for the bouncing and the splitting bubbles. The figure shows that for these types of interaction there is no relation between the shape of the signal and the interaction type. On the contrary, the penetrating bubbles do have a common feature. For the four penetrating cases that occurred during the measurements a peak was found in between the rising and falling edge of the signal. These spikes are caused by the rupture of the water film surrounding the probe (Bruun, 1995). However, similar peaks were also
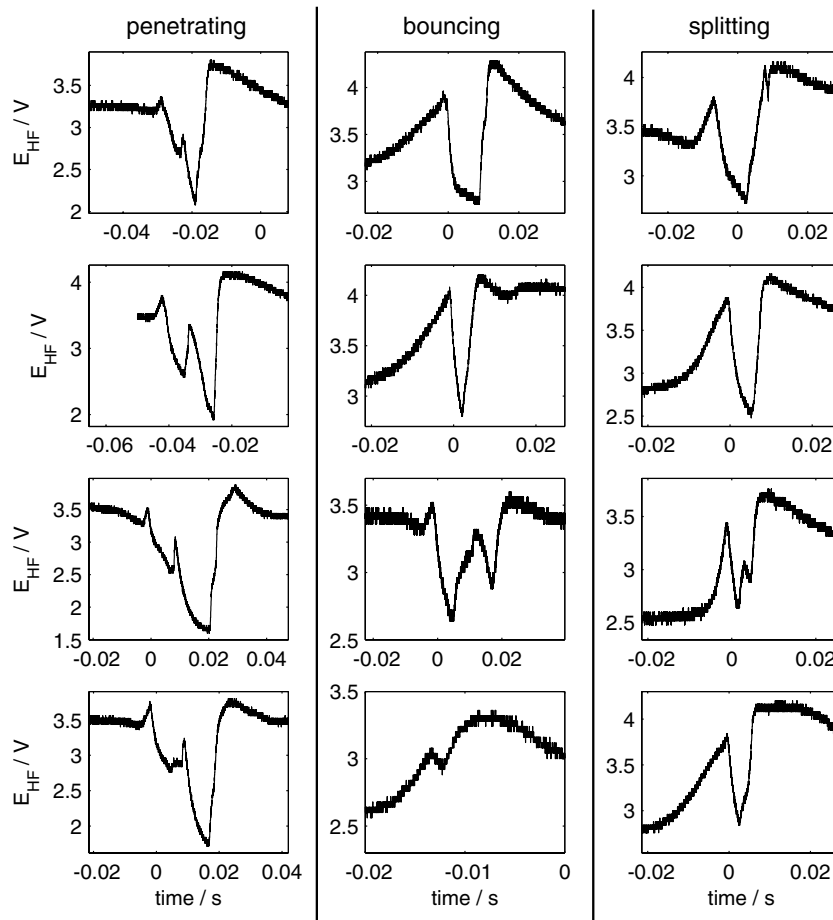
Fig. 6. Examples of hot-film signals E_{HF} belonging to penetrating bubble–probe interactions (left), bouncing bubble–probe interactions (middle), and splitting bubble–probe interactions (right) vs. time.

observed for some bouncing and splitting bubbles. Therefore we conclude that from the hot-film signal one cannot rigorously deduce the type of interaction in the present counter-current condition.

In general, a hot-film signal of a bubble–probe interaction can be divided into three parts, namely the rise of the signal just before interaction (I: pre-contact), the part between the decrease and the increase of the signal caused by the arrival and departure of the bubble (II: contact), and the settling to the initial value of the hot-film signal (III: post-contact). The Roman numbers in Fig. 3 refer to the different parts. We present the results on the shapes of the hot-film signals on the basis of these three parts.

Part I. *Pre-contact:* The first part of the signal consists of an increase. This increase originates from the water that is pushed away in front of the bubble approaching the hot-film, leading to a velocity reduction in the downflow geometry we are analyzing. We note, however, that in Fig. 6 this increase is not always seen.

Part II. *Contact:* In part II of the signal most of the variation is found. Comparing the high-speed camera images with the hot-film signal we observed that the points *a* and *b* in Fig. 3 coincide with the arrival and departure of the bubble on the probe, respectively. This finding is in agreement with earlier results (Serizawa et al., 1983; Bruun, 1995). If there is a peak in the signal that is caused by rupture of a water film on the probe, it can be found in this part of the signal.

Part III. *Post-contact:* At the moment a bubble has left the probe, basically two types of signals were observed. The first is a signal decreasing towards its initial level. The second is a signal that shows oscillations as can be seen in Fig. 7. Similar oscillations have been observed in turbulent bubbly flow (Rensen et al., in press), see Fig. 8. The frequencies of these oscillations have the same order of magnitude as the frequencies of the bubble surface oscillations found and quantitatively analyzed by de Vries et al. (2002). Therefore we assume that these fluctuations in the hot-film signal are caused by velocity changes of the water due to the surface oscillations of the bubbles.
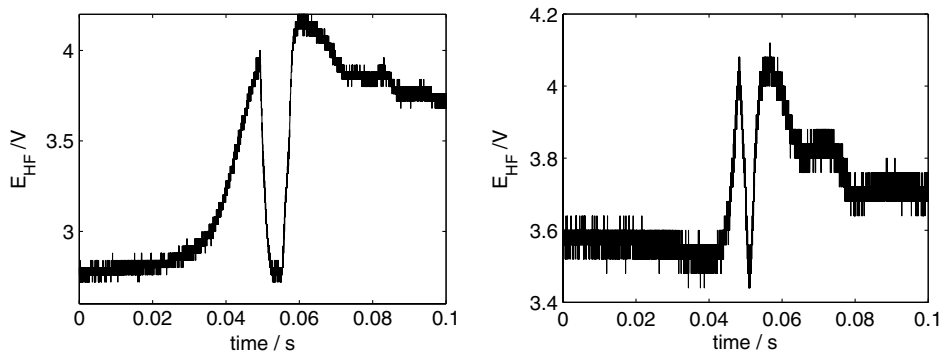

Fig. 7. Hot-film signals that contain oscillations in part III. The frequency of the oscillation in the signal on the left is about 100 Hz and from that on the right is 50 Hz. The oscillations in the signal originate from shape oscillations of the detaching bubbles, see de Vries et al. (2002).
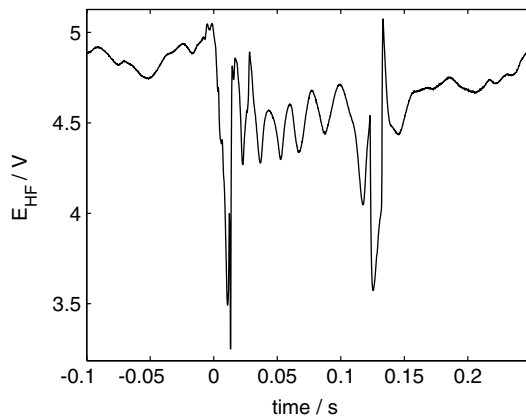

Fig. 8. Example of a hot-film signal E_{HF} during two succeeding bubble–probe interactions in a turbulent bubbly flow vs. time. After the first interaction oscillations in the hot-film signal can be observed. The frequency of the oscillation in between the two bubble–probe interactions is about 56 Hz.

It is clear that part II of the signal does not contain any information on the water velocity. Whether part III does contain reliable information about the water velocity in the wake of the bubble is a subject of discussion in the literature. Bremhorst and Gilmore (1976), Serizawa et al. (1983), and Hamad and Bruun (2000) state that part III does not represent a velocity signal. On the contrary, Ellingsen et al. (1997) state that part III does contain relevant information on the water velocity. As we did not measure the water velocity with a second velocity measurement device, we cannot conclude on this. However, we can add to the discussion that the water velocity estimate may be affected by the oscillations shown in Figs. 7 and 8.

4.3. Residence time estimate

Considering the shape deformations of the bubbles shown in Fig. 5, it may be expected that the measurement of their residence times gets biased. In Fig. 9 one can see a number of hot-film signals. The lines in this figure denote the arrival and departure time of a bubble obtained from the high-speed imaging using the model described in Section 3.3. The figure shows that the estimates of the residence times obtained from the hot-film signal is typically shorter than the estimates of the residence times obtained from the extrapolation of the bubble's path before the collision with the probe. The reason is that in most cases the bubbles just hit the probe and then get deflected, which takes less time than a full passage without interaction would take. Note that nevertheless
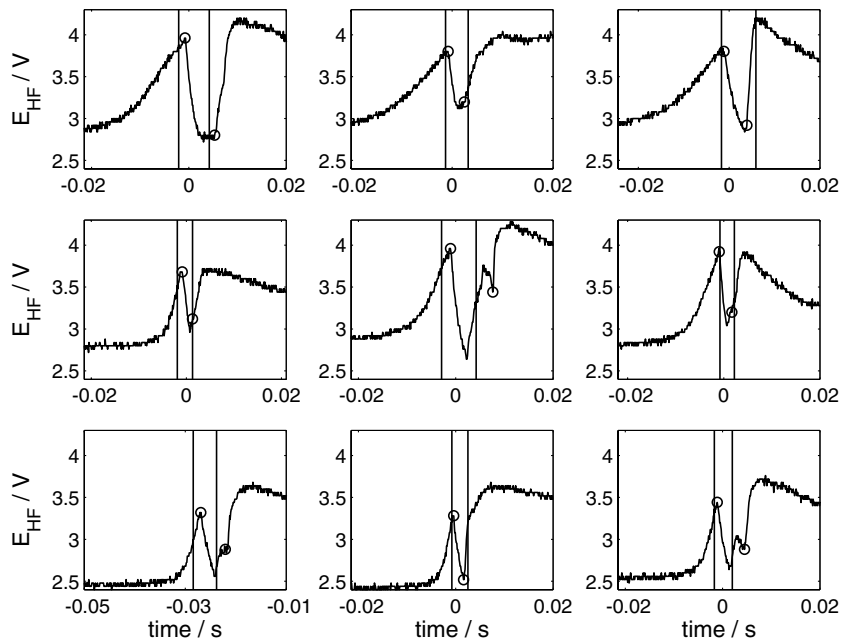

Fig. 9. Illustration of the residence times of bubbles on the probe as one would expect taking into account the shape, the position and the velocity of the bubbles before interaction. The vertical lines label the expected arrival and departure times of the bubbles based on the image sequence. The circles denote the events *a* and *b* as defined in Fig. 3. Their location is obtained by a threshold on the signal's derivative. In the figures the hot-film signal E_{HF} is plotted vs. time.
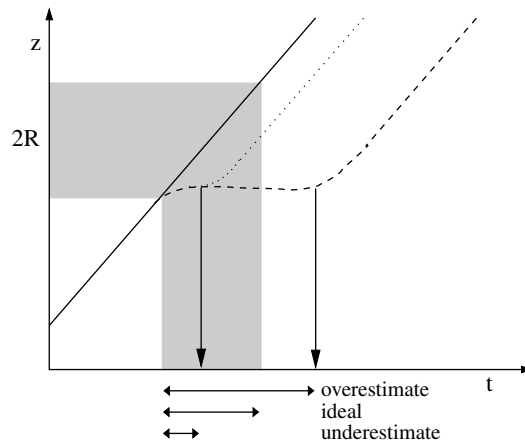
Fig. 10. Schematic illustration of the horizontal position z of a bubble vs. time t during bubble–probe interaction. The gray area indicates the residence time t_{model} or the penetration length $2R$ of a bubble that one would expect if the bubble path does not get disturbed due to the interaction. The straight line indicates the path of the bubble center of such an undisturbed bubble. The dotted and the dashed lines indicate respectively the path of the bubble center when a bubble does get deflected from the probe before or after t_{model} is reached. The figure illustrates that the residence time obtained from the hot-film signal may be over- or underestimated while the velocity of the bubble is diminished due to the interaction.

the bubbles hitting the probe may get delayed, as shown in de Vries et al. (2002), but the delayed bubbles do not touch the probe long enough to reach t_{model} as residence time. This is illustrated in Fig. 10.

In Fig. 11 the ratio of the residence times obtained from the hot-film signal t_{HF} and the residence times t_{model} estimated from an extrapolation of the bubble's path, based on the image analysis as described in Section 3.3, are plotted as a function of the equivalent bubble radius r_{eq}, the arrival velocity of the bubble on the probe V_{in}, the ratio r_{eq}/V_{in}, and the water velocity U_{water}. The comparison between the ratio t_{HF}/t_{model} and r_{eq}/V_{in} was made as the latter is like t_{HF} and t_{model} a time measurement. The comparison between t_{HF}/t_{model} and U_{water} was made to check whether the wake behind the hot-film probe has influence on the residence time of the bubbles. In the figure only those results are shown, for which the error in the ratio (see Sections 3.3 and 3.1) was smaller than 0.5. Due to this restriction only 36 bubble–probe interactions are depicted in the figures. The figures show a spread in the ratio between the two residence times estimates. On average the value t_{HF}/t_{model} is 0.54 with a standard deviation of 0.20. Therefore we conclude that the interaction affects the bubble shape and path in such a way that on average the residence time of the bubble on the probe is lower than it would have been if the bubble path and shape had not been affected by the hot-film probe. This result is in agreement with the findings of Wang et al. (1987). As a consequence, the gas fraction estimate according Eq. (2) leads to incorrect, namely too low, results in our flow situation. Fig. 11 does not show a relation between the ratio of the time differences and the sizes, the velocities, or the ratio of the sizes and the velocities of the bubbles. We cannot conclude on the influence of the water velocity on the residence time as we only obtained t_{HF}/t_{model} for a very limited number of interactions for the higher water velocities within an accuracy of 0.5.
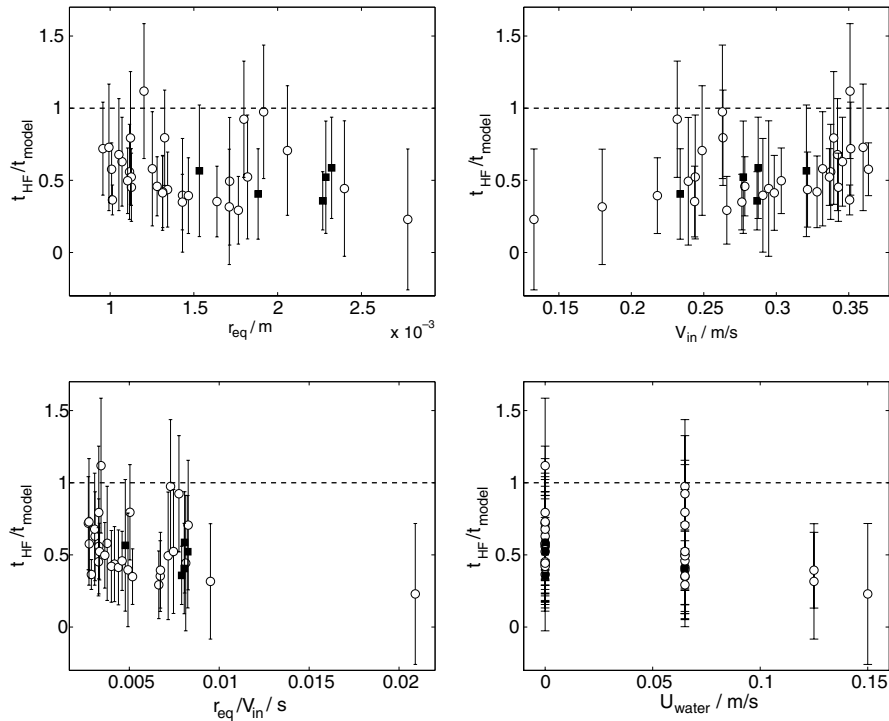
Fig. 11. Top left: Ratio of the estimate of the residence time t_{HF} as obtained from the hot-film signal and the residence time t_{model} as obtained by the model described in Sections 3.2 and 3.3 vs. the equivalent bubble radius r_{eq}. Top right: Ratio of t_{HF}/t_{model} vs. the arrival velocity V_{in} of the bubbles on the probe. Bottom left: Ratio of t_{HF}/t_{model} vs. the ratio r_{eq}/V_{in}. Bottom right: Ratio of t_{HF}/t_{model} vs. the mean water velocity U_{water} The bouncing interactions are denoted by circles and the splitting interactions by squares.

4.4. Velocity

In Fig. 12 one can see the departure velocity of the bubble V_{out} obtained from the first 15 frames after the interaction as function of the arrival velocity V_{in} of the bubble obtained from the last 15 frames before the interaction, the ratio V_{out}/V_{in} as function of the equivalent bubble radius, and the ratio V_{out}/V_{in} as function of the mean water velocity U_{water}. For the upper left and bottom plot of Fig. 12 100 bubble–probe interactions were taken into account. We could not use all the data as it was not possible to determine V_{out} for the bubbles that split during the interaction. Besides the active contour method could not successfully be applied to all the data. The value of V_{out}/V_{in} was on average 0.94 with a standard deviation of 0.12. For the upper right plot of Fig. 12 only the results are shown for which the error in the bubble size was smaller than 0.1 mm. This plot shows that there is no strong correlation between the ratio of the velocities and the bubble size. The bottom plot shows that the magnitude of the spread of V_{out}/V_{in} increases as U_{water} increases. This indicates that the wake of the probe has an effect on the bubble velocity. The plots do not only show that on average the bubble is slowed down due to the interaction, but also that there is quite some scatter in the ratio. Sometimes V_{out} is even larger than V_{in}. We do not have an explanation for this increase of the bubble velocity. However, we conclude that in our
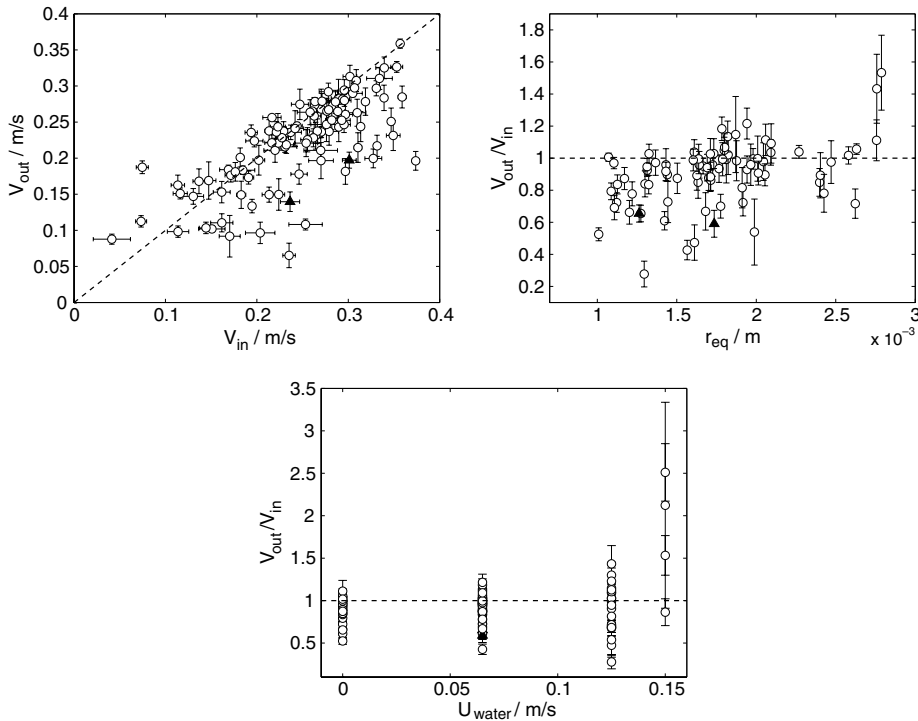
Fig. 12. Top left: the departure velocity of a bubble from the hot-film probe V_{out} vs. the arrival velocity of a bubble on the hot-film probe V_{in}. Top right: the ratio V_{out}/V_{in} vs. the equivalent bubble radius r_{eq}. Bottom: The ratio V_{out}/V_{in} vs. the mean water velocity U_{water}. The bouncing interactions are denoted by circles and the penetrating interactions by triangles.

flow situation we cannot obtain the bubble velocity accurately from the hot-film signal as the velocity of the bubble is sometimes changed considerably during the interaction.

5. Conclusions

In this paper, the interaction of a hot-film anemometer with rising bubbles in a downward water flow with mean water velocities varying from 0 to 0.15 m/s is investigated. The bubbles had equivalent radii of 0.4–2.8 mm. Simultaneous stereoscopic high-speed imaging and recording of the corresponding hot-film signal allowed for a detailed study of the interaction.

The main findings are:

- Three different types of interaction were found, i.e. penetrating, bouncing, and splitting.
- The shape variability of the hot-film signals is large. It was observed that it is not possible to obtain the type of interaction from the shape of the hot-film signal.
- The gas fraction estimate from the hot-film signal as suggested by Bruun (1995), leads to erroneous results in our flow situation due to the deformation of the bubbles' shapes and paths during the interaction. These deformations bias the residence times of the bubbles on the probe.

We did not observe a relation between the change of the residence times and the bubble sizes, or velocities.
- In our setup it is not possible to estimate the bubble velocity accurately from the hot-film signal based on the residence time as it is changing considerably during the interaction. The spread in the magnitude of the change of the velocity increases as the downward water velocity increases.

Finally, we would like to stress that although in the analyzed downflow with uprising bubbles it turned out not to be possible to accurately estimate the bubble velocity and size, this may be possible for other flow situations. The same holds for the gas fraction estimate. Independent on the flow geometry a hot-film probe of course remains a valuable instrument to measure *water* velocities.

Acknowledgments

References

Benk, H., Schmidt, T., Loth, R., 2001. Investigations of static and dynamic interactions between bubbles and x-hot-film probes. Meas. Sci. Technol. 12, 119–130.

Bremhorst, K., Gilmore, D.B., 1976. Response of hot-wire anemometer probes to a stream of air bubbles in a water flow. J. Phys. E: Sci. Instr. 9, 347–352.

Bruun, H.H., 1995. Hot-Wire Anemometry: Principles and Signal Analysis. Oxford University Press, New York.

Cipolla, R., 1998. The visual motion of curves and surfaces. Philos. T. Roy. Soc. A 356, 1103–1118.

de Vries, J., Luther, S., Lohse, D., 2002. Induced bubble shape oscillations and their impact on the rise velocity. Eur. Phys. J. B 29, 503–509.

Delhaye, J.M., 1969. Hot-film anemometry in two-phase flow. In: 11th ASME/AICHE Heat Transfer Conf. on Two-Phase Flow Instrumentation. ASME, Minneapolis, Minnesota, pp. 58–69.

Ellingsen, K., Risso, F., Roig, V., Suzanne, C., 1997. Improvements of velocity measurements in bubbly flows by comparison of simultaneous hot-film and laser-Doppler anemometry signals. In: Proc. ASME FLuid Eng. Div. Summer Meeting, Paper 97–3529. Vancouver, Canada.

Farrar, B., Bruun, H.H., 1996. A computer based hot-film technique used for flow measurements in a vertical kerosene–water pipe flow. Int. J. Multiphase Flow 22, 733–751.

Goldstein, R.J., 1996. Fluid Mechanics Measurements. Taylor & Francis, Washington.

Hamad, F.A., Bruun, H.H., 2000. Evaluation of bubble/drop velocity and slip velocity by a single normal hot-film probe placed in a two-phase flow. Meas. Sci. Technol. 11, 11–19.

Herringe, R.A., Davis, M.R., 1974. Detection of instantaneous phase changes in gas–liquid mixtures. J. Phys. E: Sci. Instr. 7, 807–812.

Kass, M., Witkin, A., Terzopoulos, D., 1987. Snakes—active contour models. Int. J. Comput. Vision 1, 321–331.

Lance, M., Bataille, J., 1991. Turbulence in the liquid phase of a uniform bubbly air–water flow. J. Fluid Mech. 222, 95.

Liu, T.J., 1997. Investigation of the wall shear stress in vertical bubbly flow under different bubble size conditions. Int. J. Multiphase Flow 23, 1085–1109.

Luther, S., Rensen, J., Guet, S., 2004. Bubble aspect ratio and velocity measurement using a four-point fiber-optical probe. Exp. Fluids 36, 326–333.

Press, W.H., Teukolsky, S.A., Vetterling, W.T., Flannery, B.P., 1992. Numerical Recipes in C, The Art of Scientific Computing. Cambridge University Press.

Rensen, J., Luther, S., Lohse, D., in press. The effect of bubbles on developed turbulence. J. Fluid Mech.

Serizawa, A., Tsuda, K., Michiyoshi, I., 1983. Real-time measurement of two-phase flow turbulence using a dual-sensor anemometry. In: Delhaye, J.M., Cognet, G. (Eds.), Proc. Symp. on Measuring Techniques in Gas–Liquid Two-Phase Flows. Springer-Verlag, Nancy, France, pp. 495–523.

Tsai, R.Y., 1987. A versatile camera calibration technique for high-accuracy 3D machine vision metrology using off-the-shelf tv cameras and lenses. IEEE Journal of Robotics and Automation RA 3, 323–344.

Wang, G., Ching, C.Y., 2001. Measurement of multiple gas-bubble velocities in gas–liquid flows using hot-film anemometry. Exp. Fluids 31, 428–439.

Wang, S.K., Lee, S.J., Jones Jr., O.C., Lahey Jr., R.T., 1987. 3-D turbulence structure and phase distribution measurements in bubbly two-phase flows. Int. J. Multiphase Flow 13, 327–343.